

## **Novel molecular “add-on” based on Evans Blue confers superior pharmacokinetics and transforms drugs to theranostic agents**

Haojun Chen<sup>1,2,\*</sup>, Orit Jacobson<sup>2,\*,§</sup>, Gang Niu<sup>2</sup>, Ido D. Weiss<sup>3</sup>, Dale O. Kiesewetter<sup>2</sup>, Yi Liu<sup>2</sup>, Ying Ma<sup>2</sup>, Hua Wu<sup>1,§</sup> and Xiaoyuan Chen<sup>2,§</sup>

1. Department of Nuclear Medicine, Xiamen Cancer Hospital of the First Affiliated Hospital of Xiamen University, Xiamen, China.
2. Laboratory of Molecular Imaging and Nanomedicine, National Institute of Biomedical Imaging and Bioengineering, National Institutes of Health, Bethesda, Maryland, USA.
3. Laboratory of Molecular Immunology, National Institute of Allergy and Infectious Diseases, National Institutes of Health, Bethesda, Maryland, USA.

§ Corresponding authors: Orit Jacobson (orit.jacobsonweiss@nih.gov); Hua Wu (wuhua1025@163.com); Xiaoyuan Chen (shawn.chen@nih.gov)

\* These authors contributed equally to this work.

**Short Title:** Evans Blue Based Theranostics

**Conflict of Interest:** None.

**First author:**

Dr. Haojun Chen

Department of Nuclear Medicine, Xiamen Cancer Center, The First Affiliated Hospital of Xiamen University, 55 Zhenhai Rd, Xiamen, 361003, China

Email: [haojun0821@gmail.com](mailto:haojun0821@gmail.com)

**Corresponding author:**

Dr. Xiaoyuan Chen

Laboratory of Molecular Imaging and Nanomedicine (LOMIN), National Institute of Biomedical Imaging and Bioengineering (NIBIB), National Institutes of Health (NIH), 35A Convent Dr, GD937, Bethesda, MD 20892-3759

Email: shawn.chen@nih.gov

**Word count:** 5316

## ABSTRACT

One of the major design considerations for a drug is its pharmacokinetics in the blood. A drug with short half-life in the blood is less available at a target organ. Such a limitation dictates treatment with either high doses or more frequent doses, both of which may increase the likelihood of undesirable side effects. To address the need for additional methods to improve the blood half-life of drugs and molecular imaging agents, we developed an “add-on” molecule that contains three groups: (i) truncated Evans Blue (EB) dye molecule that binds to albumin with low micromolar affinity and provides prolonged half-life in the blood; (ii) a metal chelate that allows radiolabeling for imaging and radiotherapy; and (iii) a maleimide for easy conjugation to drug molecules. **Methods:** The truncated EB was conjugated with 1,4,7-triazacyclononane-triacetic acid (NOTA) or 1,4,7,10-tetraazacyclododecane-tetraacetic acid (DOTA) chelator and were denoted as NMEB and DMEB, respectively. As a proof-of-concept, we coupled NMEB and DMEB to c(RGDfK), which is a small cyclic arginine-glycine-aspartic acid (RGD) peptide for targeting integrin  $\alpha_v\beta_3$ . NMEB and DMEB were radiolabeled with  $^{64}\text{Cu}$  and  $^{90}\text{Y}$ , respectively, and tested in xenograft models. **Results:** The resulting radiolabeled conjugates showed prolonged circulation half-life and enhanced tumor accumulation in  $\alpha_v\beta_3$ -expressing tumors. Tumor uptake was markedly improved compared to NOTA or DOTA conjugated c(RGDfK). Tumor radiotherapy experiments in mice using  $^{90}\text{Y}$ -DMEB-RGD showed promising results and eliminated existing tumors. **Conclusion:** Conjugation of our novel “add-on” molecules, NMEB or DMEB, to potential tracers and/or therapeutic agents improves blood half-life and tumor uptake, and can transform such agents into theranostic entities.

**Keywords:** Evans Blue, albumin-binding, RGD peptide, integrin, theranostics,  $^{90}\text{Y}$

## INTRODUCTION

The goal of drug development is to achieve high activity and specificity for a desired biological target. Many potential pharmaceuticals that meet these criteria fail, however, as therapeutics because of unfavorable pharmacokinetics, in particular rapid blood clearance that prevents achieving therapeutic concentrations. For some drugs, administration of large or frequently repeated doses is required to achieve and maintain therapeutic levels (1), which can, in turn, increase the probability of undesired side effects. One chemical modification that delays the rate of drug clearance and has been effective for some drugs is polyethyleneglycol (PEG) addition (2). Recent studies have shown, however, that PEGylation of drugs has disadvantages, including immunogenicity caused by the development of anti-PEG antibodies, heterogeneity of the PEGylated drugs, and decreased biological activity and bioavailability of the drug (1,3).

To address the need for additional methods to improve the blood half-life of drugs and molecular imaging agents, we made use of molecules with high affinity for albumin. We previously developed a radiolabeled truncated derivative of EB that allows imaging of blood volume, due to EB's affinity for albumin (4). This result encouraged us to explore drug conjugates of EB derivatives that would use albumin as a reversible carrier for drug delivery. We hypothesized that the micromolar affinity and reversible binding of EB derivatives to albumin, would extend the half-life of the drug in blood. Additionally, slow release of the drug over time would allow continual uptake at the biological target. We demonstrated this enhanced blood half-life and drug efficacy for a derivative of exendin-4 (5,6). In order to adapt this approach to theranostic applications, we now report a novel molecule that contains the same truncated EB, a metal chelate, and a maleimide that allows conjugation to a drug or targeting moiety using appropriate chemistry (Fig. 1). We prepared analogs with NOTA or DOTA as the chelator (NMEB and DMEB,

respectively). As a proof of concept, we conjugated c(RGDfK), hereafter referred to as RGD peptide for targeting cell surface receptor integrin  $\alpha_v\beta_3$ . This integrin receptor is overexpressed in various malignancies and has a crucial role in tumor angiogenesis (7-9). We demonstrated that either NMEB-RGD or DMEB-RGD can be of use as an imaging agent and as a radiotherapeutic agent for the treatment of integrin  $\alpha_v\beta_3$ -expressing tumors. The use of these novel EB derivatives confers the potential transformation of many other drugs into theranostic agents.

## **MATERIALS AND METHODS**

## **Cell culture**

U87MG human glioblastoma, MDA-MB-435 human melanoma, and HT-29 human colorectal adenocarcinoma cell lines were purchased from the American Type Culture Collection (ATCC) and grown as recommended by ATCC.

## **Small-animal PET studies**

*In vivo* studies were conducted under an animal protocol approved by the NIH Clinical Center Animal Care and Use Committee. Positron emission tomography (PET) scans and their analysis were performed as previously described (4).

## **Integrin $\alpha_v\beta_3$ -targeted radiotherapy and response monitoring**

Multiple escalating doses of  $^{90}\text{Y}$ -NMEB-RGD were tested in U87MG tumor xenografts, when tumor volume reached 150 mm<sup>3</sup>. Mice were divided into six groups (n = 5 - 8/group) (A, saline; B,  $^{90}\text{Y}$ -NMEB-RGD 7.4 MBq; C,  $^{90}\text{Y}$ -NMEB-RGD 3.7 MBq; D,  $^{90}\text{Y}$ -NMEB-RGD 1.75 MBq; E,  $^{90}\text{Y}$ -RGD 7.4 MBq; and F,  $^{90}\text{Y}$ -RGD 1.85 MBq), and each animal received intravenous dose of  $^{90}\text{Y}$ -NMEB-RGD. Groups B-D received an additional dose at day 14 post-treatment. For HT-29 xenografts, two groups were compared; control (injected with saline) and treated (injected with 7.4 MBq of  $^{90}\text{Y}$ -NMEB-RGD). Anti-tumor efficacy was evaluated by monitoring the tumor volume and body weight every 2 days. Individual tumor size was calculated using the formula  $[0.5 \times (L \times W^2)]$ . Groups A, B, D, and E underwent both  $^{18}\text{F}$ -FDG PET imaging 3 and 10 days after the start of treatment and  $^{18}\text{F}$ -FLT PET imaging 5 and 12 days after therapy. The PET imaging protocol was similar as previously described, the only difference was 4-h fasting before  $^{18}\text{F}$ -FDG PET.

The endpoint criteria for Kaplan-Meier analysis were weight loss of more than 15%; a tumor volume > 1600 mm<sup>3</sup>; active ulceration of the tumor; and abnormal behavior indicating pain or unease.

## RESULTS

### Preparation of radiolabeled compounds

The new EB-RGD derivatives were prepared by linking the truncated EB to the lysine spacer, attaching the chelator to the  $\alpha$ -amine, attaching a maleimide to the  $\varepsilon$ -amine, and finally attaching thiolated RGD peptide to the maleimide (Fig 1). The usage of either NOTA or DOTA depended on the radionuclide to be complexed. We prepared four compounds as tests and controls for the purposes of ligand validation (Fig. 1; Supplemental Fig. 1): 1) <sup>64</sup>Cu-NMEB-RGD, which has high affinity for integrin  $\alpha_v\beta_3$  and contains an albumin binding moiety; 2) <sup>64</sup>Cu-NMEB-RAD, a control peptide with no affinity for  $\alpha_v\beta_3$  receptor (10), but retaining the albumin binding moiety; 3) <sup>64</sup>Cu-NOTA-RGD, which has high affinity for integrin  $\alpha_v\beta_3$  receptor, but lacks the albumin binding moiety; and 4) <sup>64</sup>Cu-NEB, which is the albumin binding moiety (4,11).

### *In vitro* characterization of NMEB-RGD

The binding affinity of NMEB-RGD to integrin  $\alpha_v\beta_3$  was compared with RGD in competition assays using U87MG cells. Preliminary experiments showed that competition with NMEB-RGD in the presence of human serum albumin (HSA) did not reach equilibrium at 1h, hence further experiments were carried out at 4 h. The IC<sub>50</sub> values for NMEB-RGD and RGD were 74.1 ± 28.2 nM and 85.2 ± 14.0 nM (Fig. 2A) when competed against <sup>64</sup>Cu-RGD (Specific activity 6.6 GBq/μmol) at 4 h. The binding affinity of NMEB-RGD to albumin (2.34 ± 1.38 μM,

Fig. 2B) was comparable to the published binding affinity of Evans Blue to albumin ( $\sim 2.5 \mu\text{M}$ ) (12,13).

Changing the chelator from NOTA to DOTA did not change the binding affinity towards integrin  $\alpha_v\beta_3$  ( $\text{IC}_{50}$  of  $67.8 \pm 33.6 \text{ nM}$  for DOTA-RGD vs.  $76.6 \pm 31 \text{ nM}$  for DMEB-RGD without addition of HSA and  $185.23 \pm 121.28 \text{ nM}$  in the presence of 1% HSA, Supplemental Fig. 2A). Replacement of the glycine residue with alanine in the RGD peptide abolished its binding to the receptor (Supplemental Fig. 2B).

### **Cellular uptake and internalization**

$^{64}\text{Cu}$ -NMEB-RGD cell uptake and internalization were tested using three cell lines (U87MG, MDA-MB-435 and HT-29) which express different levels of integrin  $\alpha_v\beta_3$  (high, medium and low, respectively) (14,15).  $^{64}\text{Cu}$ -NMEB-RGD uptake at all time points was significantly higher without albumin in the medium (Fig. 2C).  $^{64}\text{Cu}$ -NMEB-RGD uptake by U87MG cells increased with longer incubation time, reaching  $1.86 \pm 0.22\%$  of total input at 4 h. For HT-29 cells, the uptake was significantly lower ( $0.76 \pm 0.03\%$ , Supplemental Fig. 3A). The specificity of  $^{64}\text{Cu}$ -NMEB-RGD for integrin  $\alpha_v\beta_3$  was tested by co-incubation with an excess amount of either RGD or NMEB-RGD (Fig. 2C). At 5 min,  $^{64}\text{Cu}$ -NMEB-RGD uptake was not due to internalization. However, at later time points, most of  $^{64}\text{Cu}$ -NMEB-RGD uptake was internalized (Fig. 2D). This phenomenon was also seen in MDA-MB-435 and HT-29 cell lines (Supplemental Figs. 3A-C). Internalization of NMEB-RGD did not induce internalization of albumin (Supplemental Fig. 3D).

### **Stability of $^{64}\text{Cu}$ -NMEB-RGD**

$^{64}\text{Cu}$ -NMEB-RGD was stable in mouse serum for up to 24 h with no significant demetalation observed (Supplemental Fig. 4A). *In vivo*, over 90% of the radioactivity was bound to the blood proteins and not extractable. Consistent with this finding, the free fraction in the plasma for  $^{64}\text{Cu}$ -NMEB-RGD was 4.2%, while that for  $^{64}\text{Cu}$ -RGD was 51%. The extracted radioactivity showed  $^{64}\text{Cu}$ -NMEB-RGD with only a small amount of a more polar component appearing at 4 h after *i.v.* administration (Supplemental Fig 4B).

### **MicroPET imaging of tumor xenografts with $^{64}\text{Cu}$ -NMEB-RGD**

Three tumor models with varying degrees of tumor vascularization and different levels of cellular integrin  $\alpha_v\beta_3$  receptor expression were selected for imaging studies. U87MG and HT-29 tumors both showed elevated vascularity as indicated by high CD31 staining, while MDA-MB-435 tumor had relatively weaker staining (Supplemental Fig. 5A). Human integrin  $\alpha_v\beta_3$  was highest in U87MG tumor tissue, followed by MDA-MB-435, and then HT-29, which showed much lower levels (Supplemental Fig. 5A). Murine integrin  $\beta_3$  (CD61) expression levels were in agreement with CD31 staining, following the order of U87MG > HT-29 > MDA-MB-435 (Supplemental Fig. 5A).

All four radiotracers were first evaluated in  $\alpha_v\beta_3$ -high U87MG xenografts.  $^{64}\text{Cu}$ -NMEB-RGD had significantly higher tumor uptake than all the other tracers at all time points ( $9.87 \pm 1.40$ ,  $14.09 \pm 1.62$  and  $16.64 \pm 1.99$  %ID/g at 1, 4 and 24 h post-injection (p.i.), respectively) (Fig. 3).  $^{64}\text{Cu}$ -NMEB-RGD uptake in the blood was relatively high at 1 h p.i. ( $9.58 \pm 0.84$  %ID/g), but significantly decreased at 4 and 24 h p.i. to  $5.73 \pm 0.67$  and  $2.46 \pm 0.25$  %ID/g, respectively, and resulted in a high tumor uptake and tumor-to-background ratio at 24 h time point (Fig. 3; Supplemental Fig. 5B and C).  $^{64}\text{Cu}$ -NMEB-RGD uptake in both MDA-MB-435 and HT-29 xenografts was significantly lower than that in U87MG at all time points (Supplemental Fig. 6A

and B). When an excess of RGD was co-injected, the tumor uptake decreased significantly at 1 h p.i. ( $5.77 \pm 0.08$  %ID/g,  $P = 0.017$ ). At 4 h p.i. the tumor uptake increased to  $11.1 \pm 0.05$  %ID/g, and this uptake further increased at 24 h p.i. to values similar to those of  $^{64}\text{Cu}$ -NMEB-RGD (Fig. 3). Co-injection using excess amount of unlabeled NMEB-RGD successfully blocked tumor uptake at all time points by 55-65% (Fig. 3; Supplemental Fig. 5C). PET studies were validated by biodistribution at 24 h (Supplemental Fig. 7A).

As expected,  $^{64}\text{Cu}$ -NOTA-RGD was rapidly cleared from the blood through the urinary tract and exhibited low accumulation in the tumor ( $1.29 \pm 0.17$ ,  $1.15 \pm 0.07$ , and  $1.06 \pm 0.03$  %ID/g at 1, 4 and 24 h p.i., respectively). The non-binding tracer,  $^{64}\text{Cu}$ -NMEB-RAD, had low tumor accumulation (approximately 6 %ID/g) at all the time points examined. Its uptake in the blood was significantly higher than  $^{64}\text{Cu}$ -NMEB-RGD at all the time points (10-12 % ID/g up to 4 h p.i and  $3.7 \pm 0.3$  %ID/g at 24 h p.i.).  $^{64}\text{Cu}$ -NEB had the highest accumulation in the blood at all time points while uptake in the tumor was only slightly higher than  $^{64}\text{Cu}$ -NMEB-RAD (6-7 %ID/g up to 4 h p.i. and approximately 8 %ID/g at 24 h p.i.) (Fig. 3; Supplemental Fig. 5C).

The blood and heart uptake were similar with all the three models (Supplemental Fig. 7B). In order to assess the portion of the tumor uptake that is due to specific receptor binding, rather than vascularity or enhanced permeability and retention (EPR) effect, we injected the blood pool imaging tracer,  $^{64}\text{Cu}$ -NEB to MDA-MB-435 and HT-29 xenografts.  $^{64}\text{Cu}$ -NEB uptake was in correlation with CD31 and CD61 staining, following the order of U87MG > HT-29 > MDA-MB-435 (Supplemental Fig. 7C).

### **$^{90}\text{Y}$ radiotherapy**

The unique pharmacokinetics of NMEB-RGD encouraged us to apply this chemical formulation for integrin  $\alpha_v\beta_3$ -targeted radiotherapy. In order to allow complexation of the

radiotherapeutic isotope  $^{90}\text{Y}$ , the NOTA group of NMEB was replaced with DOTA to give DMEB. Anti-tumoral radiotherapy efficacy was evaluated in U87MG tumor-bearing mice treated as indicated in Fig. 4A. At day 6 post treatment, significant differences between the groups were evident from the tumor growth curves (Fig. 4B). The tumor volumes from all  $^{90}\text{Y}$ -DMEB-RGD treated mice (groups B-D) were significantly lower ( $P < 0.01$ ) than the control group A (Fig. 4B). Moreover, starting from day 8 after the treatment, significant differences in the tumor volume were observed between all three groups of  $^{90}\text{Y}$ -DMEB-RGD and groups E-F (Fig. 4B). These differences increased over time, and tumors of mice injected with 7.4 MBq of  $^{90}\text{Y}$ -DMEB-RGD showed partial regression by day 8 (group B, Fig. 4B). A second injection of 7.4 MBq  $^{90}\text{Y}$ -DMEB-RGD, reduced the tumor volume significantly ( $P = 0.01$  at day 20 and  $P = 0.0003$  at day 22, Fig. 4B) and the tumors almost disappeared by day 30 post initial treatment. Minor tumor volume reduction, which lasted for several days after the second injection, was observed in group C (3.7 MBq dose), but then the tumor volume increased once more (Fig. 4B). No effect on the tumor volume was observed for group D (which received a dose of 1.75 MBq). No systemic toxicity due to radiotherapy was observed by monitoring animal body weight (Fig. 4C). Kaplan-Meier curves based on the protocol end points showed significant differences ( $P < 0.01$ ) for groups B-D in comparison to groups A, E, and F. For group B the survival was 100% up to 30 days post initial treatment (Fig. 4D).

We tested the therapeutic efficacy of 7.4 MBq  $^{90}\text{Y}$ -DMEB-RGD in HT-29 mice (Supplemental Figs. 8A and 8B) compared to saline injected controls. The tumor volume between the treated group and the control was similar up to 8 days post-treatment, and then the treated tumors started to grow at a slower rate than the control. As a result,  $^{90}\text{Y}$ -DMEB-RGD-targeted

radiotherapy led to a delay of tumor growth in HT-29 tumor xenografts, rather than tumor shrinkage as shown in U87MG tumors (Figs. 4C; Supplemental Fig. 8A).

During treatment, we evaluated tumor metabolism using appropriate PET tracers.  $^{18}\text{F}$ -FDG PET imaging 3 days post-injection of  $^{90}\text{Y}$  showed decreased uptake, indicating reduced glucose utilization, only for the groups injected with  $^{90}\text{Y}$ -DMEB-RGD (Fig. 5A). However, repeating this scan 10 days post-treatment showed significantly decreased metabolism only for group B (Fig. 5A).  $^{18}\text{F}$ -FLT PET imaging, and indicator of cellular replication, was conducted 5 and 12 days after initial treatment and showed significantly less  $^{18}\text{F}$ -FLT uptake for group B (treated with 7.4 MBq of  $^{90}\text{Y}$ -DMEB-RGD) compared to controls at both imaging times, suggesting lower proliferation of the tumor in these mice (Fig. 5B).

### **Tumor biology after $^{90}\text{Y}$ radiotherapy**

CD31 staining to evaluate tumor vasculature, Ki-67 staining to evaluate tumor proliferation, and terminal deoxynucleotidyl transferase dUTP nick end labeling (TUNEL) staining to determine the DNA damage were conducted on excised tumors for all six groups (A-F). For groups A, E and F, with large necrotic areas, we evaluated live cells on the tumor rim. As shown in Fig. 5C, the tumor vasculature in group B (injected with 7.4 MBq of  $^{90}\text{Y}$ -DMEB-RGD) was the lowest of all groups. Consistent with  $^{18}\text{F}$ -FLT PET imaging, a relatively high percentage of cells stained positively for Ki-67 in groups A, and C-F, while significantly reduced cell proliferation was observed in group B (Fig. 5C). Compared with the other 5 groups, group B showed considerably more cell apoptosis, depicted by TUNEL staining (Fig. 5C). Hematoxylin and eosin staining showed that most of the tumor area in group B was already necrotic after two doses of  $^{90}\text{Y}$ -DMEB-RGD treatment, whereas tumors from the other 5 groups had necrotic areas

only in the middle of the tumor, suggesting that the necrosis was due to insufficient blood supply and hypoxia (Fig. 5C).

## DISCUSSION

One of the major design considerations for a drug is its pharmacokinetics in the blood. A drug with short half-life in the blood is less available at a target organ. Such a limitation dictates treatment with either high doses or more frequent doses, both of which may increase the likelihood of undesirable side effects. We describe here a novel EB derivative that, upon conjugation to therapeutic or targeting agents, results in enhanced blood half-life. In addition, the design includes the ability to attach a chelator for radiometals. Thus, it allows the transformation of a drug into a theranostic agent, for use as both an imaging and therapeutic agent.

The reversible binding of EB to albumin has been well documented with a stoichiometry of 8-14 dye molecules per molecule of albumin (16,17). The binding of EB to albumin has been exploited by others to quantify protein leakage as an indicator of increased vascular permeability (17,18). Additionally, our lab has utilized a truncated version of EB to develop a blood volume imaging agent for use in PET (4). We subsequently postulated that the binding properties of EB and its derivatives to albumin can be used to retain drugs/tracers in the blood. We prepared a truncated EB derivative of exendin-4 that proved effective for long term glucose control (5).

In this study, we designed a tracer that incorporated: (i) an albumin binding motif based on EB, (ii) a chelator for easy labeling with radioactive metal isotopes for imaging and/or radiotherapy, and (iii) a biomolecule binding motif to give selectivity for a chosen target. As a proof of concept we chose RGD peptide as the targeting biomolecule. This cyclic peptide has been

shown to: (i) specifically bind integrin  $\alpha_v\beta_3$  with high affinity (nM range), (ii) rapidly disappear from the blood circulation, and (iii) become internalized by receptor-mediated endocytosis (19,20).

Other albumin binding molecules have been utilized to modulate pharmacokinetics for therapeutic purposes (13). Prof. Neri's group have worked extensively to identify albumin binding molecules by screening chemical libraries, one of which was 4-(*p*-iodophenyl)butanoic acid (21,22), which was evaluated by Müller *et al.* on its employment as a means for the improvement of folate receptor binding tracer/radiotherapy agent (23). Subsequent labeling with  $^{177}\text{Lu}$  for radiotherapy of tumor-bearing mice gave promising results (23,24). Although Müller *et al.* did not explicitly mention that their modifications can be used for labeling other biomolecules, it seemed to be chemically feasible.

The hypothesis that albumin can serve as a pool and allow slow release of NMEB-RGD was first supported in binding assays with  $\alpha_v\beta_3$ -expressing cells. In the absence of albumin in the binding buffer, there was no difference between NMEB-RGD and RGD in apparent binding affinity to these cells. In the presence of albumin, time to equilibrium was increased but binding affinities at equilibrium remained similar for both compounds (Fig. 2A). We propose a mechanism in which the concentration of free NMEB-RGD is initially reduced, due to receptor mediated internalization, but equilibrium is maintained by slow release of the albumin bound NMEB-RGD. To support this hypothesis, we performed internalization assays, and found that most of the  $^{64}\text{Cu}$ -NMEB-RGD was internalized, with only a small fraction bound to the surface (Fig. 2D). This mechanism is also supported by the observation that FITC-albumin was not internalized in the presence of NMEB-RGD (Supplemental Fig. 3D).

*In vivo* experiments with  $^{64}\text{Cu}$ -NMEB-RGD were used to evaluate the specific uptake into tumor. Initially, we used  $^{64}\text{Cu}$ -NEB and  $^{64}\text{Cu}$ -NMEB-RAD to evaluate the EPR effect and,

compared with  $^{64}\text{Cu}$ -NMEB-RGD, we found that EPR is responsible for about 35% of tumor uptake (Fig. 3; Supplemental Fig. 5C). Blocking experiments were done with both RGD and NMEB-RGD, showed that RGD, which does not bind to albumin, blocks  $^{64}\text{Cu}$ -NMEB-RGD accumulation in the tumor at 1 h. However, due to rapid turnover of the receptor and fast clearance of RGD from the blood, the blocking effect is limited to early time points after injection, and does not block the  $^{64}\text{Cu}$ -NMEB-RGD that is slowly released from albumin over longer time period. At 24 h the accumulation of  $^{64}\text{Cu}$ -NMEB-RGD with and without RGD blocking was similar (Fig. 3; Supplemental Fig. 5C). Blocking with NMEB-RGD, on the other hand, successfully inhibited  $^{64}\text{Cu}$ -NMEB-RGD accumulation in the tumor, reducing the observed %ID/g by about 65%.

The residual 35% is accredited to EPR or other non-specific uptake mechanisms, since these are consistent with EPR estimates from the non-targeting NMEB-RAD. The three-fold enhanced uptake of  $^{64}\text{Cu}$ -NMEB-RGD compared to  $^{64}\text{Cu}$ -NMEB-RAD demonstrates the benefit of targeted delivery. The proportion of non-specific binding will preclude us from using this tracer to quantitatively estimate integrin receptor' levels, however it remains useful as an imaging agent to estimate the expected uptake of the analogous radiotherapeutic.

Uptake of  $^{64}\text{Cu}$ -NMEB-RGD by neovasculature can be estimated by comparing uptake in  $\alpha_v\beta_3$ -low HT-29 and  $\alpha_v\beta_3$ -high U87MG tumors. Both tumors have high levels of murine vascular integrin expression. HT-29 tumor uptake was about half that of U87MG tumor. Since we ascribe 35% of tumor uptake to the EPR effect, based on observed, non-receptor mediated NEB uptake, the remaining 15% of HT-29 uptake may be due to uptake by the neovasculature. However, these are crude calculations and further experiments would be required to evaluate the contribution of neovasculature and neoangiogenesis to  $^{64}\text{Cu}$ -NMEB-RGD uptake.

A very important observation from the *in vivo* experiment was that when we compared  $^{64}\text{Cu}$ -NMEB-RGD and  $^{64}\text{Cu}$ -RGD we saw about a 10-fold increase in accumulation of radioactivity in the tumor (Supplemental Fig. 5B). This high accumulation is a direct proof that using the same molar amount of the tracer we received significantly higher accumulation in the target organ, which was our aim. This higher uptake was mediated by the slower pharmacokinetics, afforded by albumin binding, and resulted in enhanced radionuclide uptake that provided higher imaging contrast. Moreover, the high accumulation of the tracer in the target organ resulted in enhanced sensitivity, enabling detection of tumors that express lower amounts of integrin, which might have been detected as “ $\alpha_v\beta_3$ -negative” otherwise.

The enhanced uptake with  $^{64}\text{Cu}$ -NMEB-RGD for imaging predicted that radiotherapy could be conducted with a suitably prepared analog. We chose to use the therapeutic radionuclide  $^{90}\text{Y}$ . Since NOTA does not chelate Y, the EB derivative was resynthesized with a DOTA chelator for the radiotherapeutic isotope  $^{90}\text{Y}$ ; the resulting analog was denoted as DMEB-RGD. DOTA provides strong and stable chelation with  $^{90}\text{Y}$  (25,26); but is not optimal for  $^{64}\text{Cu}$ .

Previous reports on  $\alpha_v\beta_3$  as a radiotherapeutic target included using  $^{90}\text{Y}$ -labeled RGD and labeling a specific antibody with  $^{90}\text{Y}$  (27-30). The results with  $^{90}\text{Y}$ -RGD were not encouraging, as mentioned above, perhaps because the peptide was cleared rapidly from the blood and showed very low tumor residence time. The antibody, on the other hand, had a beneficial effect on tumor size reduction and mouse longevity; however, the long time that is required for clearance of antibodies from the blood might result in high absorbed dose in non-tumor tissues.

Tumor-bearing mice were treated with various doses of  $^{90}\text{Y}$ -DMEB-RGD on day 0 and day 14. Therapeutic response to the radiotherapy was scored based on both survival and changes in tumor volume. At a high dose of 7.4 MBq, the tumors shrank to almost unobservable size (Fig.

4B). They also showed reduced uptake of  $^{18}\text{F}$ -FDG and  $^{18}\text{F}$ -FLT, suggesting lower proliferation of tumor cells and lower metabolism (Figs. 5A and 5B). TUNEL staining confirmed that the tumors of the group that received the highest dose of  $^{90}\text{Y}$ -DMEB-RGD underwent apoptosis. The therapeutic response was also confirmed by immunostaining for CD31 (a vascularization marker) and Ki67 (a proliferation marker).

## CONCLUSION

We have developed a novel molecule containing an albumin binding motif, a chelator for radiometals, and a point of attachment for drugs or targeting molecules. The chelator is selected based on the desired radiometal and we used both NOTA and DOTA. This novel molecule, when conjugated with a drug or targeting molecule, transforms the attached compound into a theranostic agent, which enables radiolabeling for imaging and radiotherapy. The major feature is the inclusion of an EB-derived albumin binding moiety that affects the pharmacokinetics in a very positive manner to enhance tumor uptake. The increased uptake provides high contrast for diagnostic imaging purposes and increases radiotherapeutic dose delivery. The results shown here for radiolabeled NMEB-RGD and DMEB-RGD are very promising and should be further investigated and confirmed with other therapeutic agents.

## **ACKNOWLEDGMENTS**

The authors gratefully acknowledge the National Natural Science Foundation of China (81471684 and 81371596) and the Intramural Research Program, National Institute of Biomedical Imaging and Bioengineering, National Institutes of Health. Haojun Chen was partially funded by the China Scholarship Council (CSC).

## REFERENCES

1. Caliceti P, Veronese FM. Pharmacokinetic and biodistribution properties of poly(ethylene glycol)-protein conjugates. *Adv Drug Deliv Rev.* 2003;55:1261-1277.
2. Pedder SC. Pegylation of interferon alfa: structural and pharmacokinetic properties. *Semin Liver Dis.* 2003;23 Suppl 1:19-22.
3. Zhang F, Liu MR, Wan HT. Discussion about several potential drawbacks of PEGylated therapeutic proteins. *Biol Pharm Bull.* 2014;37:335-339.
4. Niu G, Lang L, Kiesewetter DO, *et al.* In vivo labeling of serum albumin for PET. *J Nucl Med.* 2014;55:1150-1156.
5. Liu Y, Wang G, Zhang H, *et al.* Stable Evans blue derived exendin-4 peptide for type 2 diabetes treatment. *Bioconjug Chem.* 2016;27:54-58.
6. Chen H, Wang G, Lang L, *et al.* Chemical conjugation of Evans blue derivative: A strategy to develop long-acting therapeutics through albumin binding. *Theranostics.* 2016;6:243-253.
7. Cai W, Niu G, Chen X. Imaging of integrins as biomarkers for tumor angiogenesis. *Curr Pharm Des.* 2008;14:2943-2973.
8. Haubner R, Maschauer S, Prante O. PET radiopharmaceuticals for imaging integrin expression: tracers in clinical studies and recent developments. *Biomed Res Int.* 2014;2014:871609.
9. Zhao D, Jin X, Li F, Liang J, Lin Y. Integrin  $\alpha v \beta 3$  imaging of radioactive iodine-refractory thyroid cancer using  $^{99m}\text{Tc}$ -3PRGD2. *J Nucl Med.* 2012;53:1872-1877.
10. Yang J, Guo H, Miao Y. Technetium-99m-labeled Arg-Gly-Asp-conjugated alpha-melanocyte stimulating hormone hybrid peptides for human melanoma imaging. *Nucl Med Biol.* 2010;37:873-883.
11. Zhang J, Lang L, Zhu Z, Li F, Niu G, Chen X. Clinical Translation of an albumin-binding PET radiotracer  $^{68}\text{Ga}$ -NEB. *J Nucl Med.* 2015;56:1609-1614.
12. Peters TJ. All About Albumin. *Academic Press.* 1995;1st Edition (ISBN: 978-0-12-552110-9):76-132.
13. Liu Z, Chen X. Simple bioconjugate chemistry serves great clinical advances: albumin as a versatile platform for diagnosis and precision therapy. *Chem Soc Rev.* 2016;45:1432-1456.

14. Gianni T, Cerretani A, Dubois R, *et al.* Herpes simplex virus glycoproteins H/L bind to cells independently of  $\alpha\beta 3$  integrin and inhibit virus entry, and their constitutive expression restricts infection. *J Virol.* 2010;84:4013-4025.
15. Cai W, Wu Y, Chen K, Cao Q, Tice DA, Chen X. In vitro and *in vivo* characterization of  $^{64}\text{Cu}$ -labeled Abegrin, a humanized monoclonal antibody against integrin  $\alpha\beta 3$ . *Cancer Res.* 2006;66:9673-9681.
16. Rawson RA. The binding of T-1824 and structurally related diazo dyes by plasma proteins. *Amer J Physiol.* 1943;137:708.
17. Lindner V, Heinle H. Binding properties of circulating Evans blue in rabbits as determined by disc electrophoresis. *Atherosclerosis.* 1982;43:417-422.
18. Saria A, Lundberg JM. Evans blue fluorescence: quantitative and morphological evaluation of vascular permeability in animal tissues. *J Neurosci Methods.* 1983;8:41-49.
19. Garanger E, Boturyn D, Dumy P. Tumor targeting with RGD peptide ligands-design of new molecular conjugates for imaging and therapy of cancers. *Anticancer Agents Med Chem.* 2007;7(5):552-558.
20. Sancey L, Garanger E, Foillard S, *et al.* Clustering and internalization of integrin  $\alpha\beta 3$  with a tetrameric RGD-synthetic peptide. *Mol Ther.* 2009;17:837-843.
21. Trussel S, Dumelin C, Frey K, Villa A, Buller F, Neri D. New strategy for the extension of the serum half-life of antibody fragments. *Bioconj Chem.* 2009;20:2286-2292.
22. Dumelin CE, Trussel S, Buller F, *et al.* A portable albumin binder from a DNA-encoded chemical library. *Angew Chem Int Ed Engl.* 2008;47:3196-3201.
23. Muller C, Struthers H, Winiger C, Zhernosekov K, Schibli R. DOTA conjugate with an albumin-binding entity enables the first folic acid-targeted  $^{177}\text{Lu}$ -radionuclide tumor therapy in mice. *J Nucl Med.* 2013;54(1):124-131.
24. Haller S, Reber J, Brandt S, *et al.* Folate receptor-targeted radionuclide therapy: preclinical investigation of anti-tumor effects and potential radionephropathy. *Nucl Med Biol.* 2015;42:770-779.
25. Boswell CA, Sun X, Niu W, *et al.* Comparative *in vivo* stability of copper-64-labeled cross-bridged and conventional tetraazamacrocyclic complexes. *J Med Chem.* 2004;47:1465-1474.
26. Garrison JC, Rold TL, Sieckman GL, *et al.* *In vivo* evaluation and small-animal PET/CT of a prostate cancer mouse model using  $^{64}\text{Cu}$  bombesin analogs: side-by-side comparison of the CB-TE2A and DOTA chelation systems. *J Nucl Med.* 2007;48:1327-1337.

27. Liu Z, Shi J, Jia B, *et al.* Two  $^{90}\text{Y}$ -labeled multimeric RGD peptides RGD4 and 3PRGD2 for integrin targeted radionuclide therapy. *Mol Pharm.* 2011;8:591-599.
28. Janssen ML, Oyen WJ, Dijkgraaf I, *et al.* Tumor targeting with radiolabeled  $\alpha\text{v}\beta 3$  integrin binding peptides in a nude mouse model. *Cancer Res.* 2002;62:6146-6151.
29. Chen H, Niu G, Wu H, Chen X. Clinical application of radiolabeled RGD peptides for PET imaging of integrin  $\alpha\text{v}\beta 3$ . *Theranostics.* 2016;6:78-92.
30. Veeravagu A, Liu Z, Niu G, *et al.* Integrin  $\alpha\text{v}\beta 3$ -targeted radioimmunotherapy of glioblastoma multiforme. *Clin Cancer Res.* 2008;14:7330-7339.

## FIGURE LEGENDS

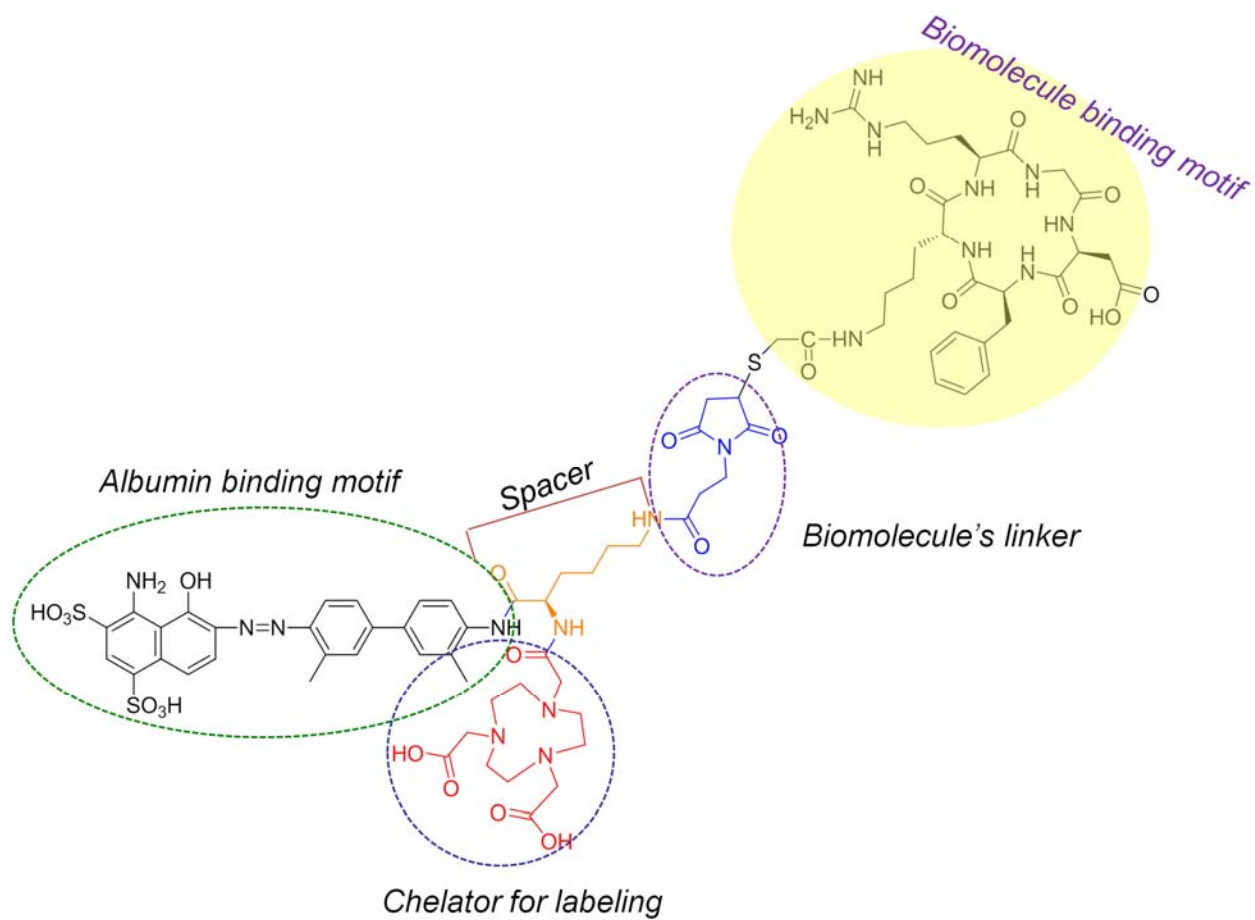


**Figure 1.** Chemical structure of NMEB-RGD.

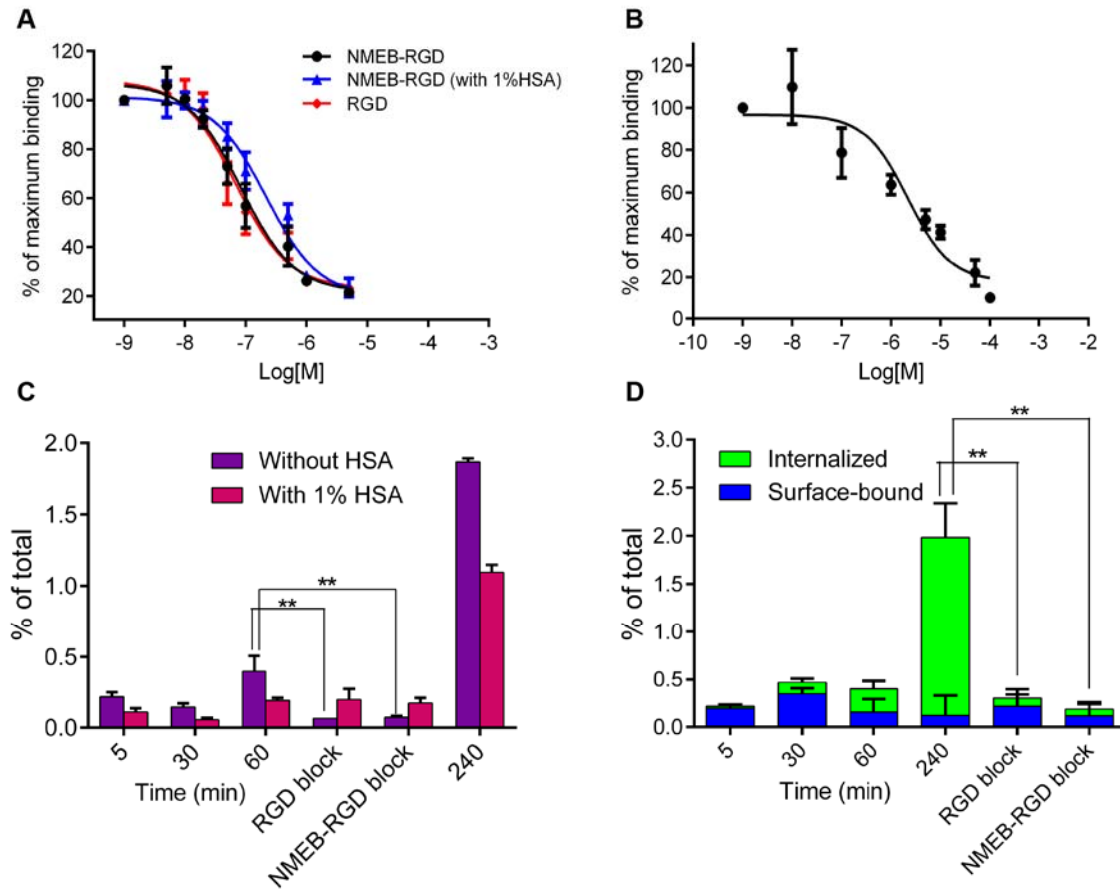


**Figure 2.** (A) Cell binding assay in U87MG cells using  $^{64}\text{Cu}$ -RGD as a competitor and 4 h incubation time. (B) Binding assay of NMEB-RGD to FITC-albumin using avidin beads. (C) Uptake of  $^{64}\text{Cu}$ -NMEB-RGD in U87MG cells without HSA (purple bars) and with 1% HSA (pink bars). Blocking studies were evaluated at 1 h. (D) Internalization of  $^{64}\text{Cu}$ -NMEB-RGD in U87MG cells. Green bars represent the internalized and the blue bars represent surface bound  $^{64}\text{Cu}$ -NMEB-RGD. Blocking studies were evaluated at 4 h.  $**P < 0.01$ .

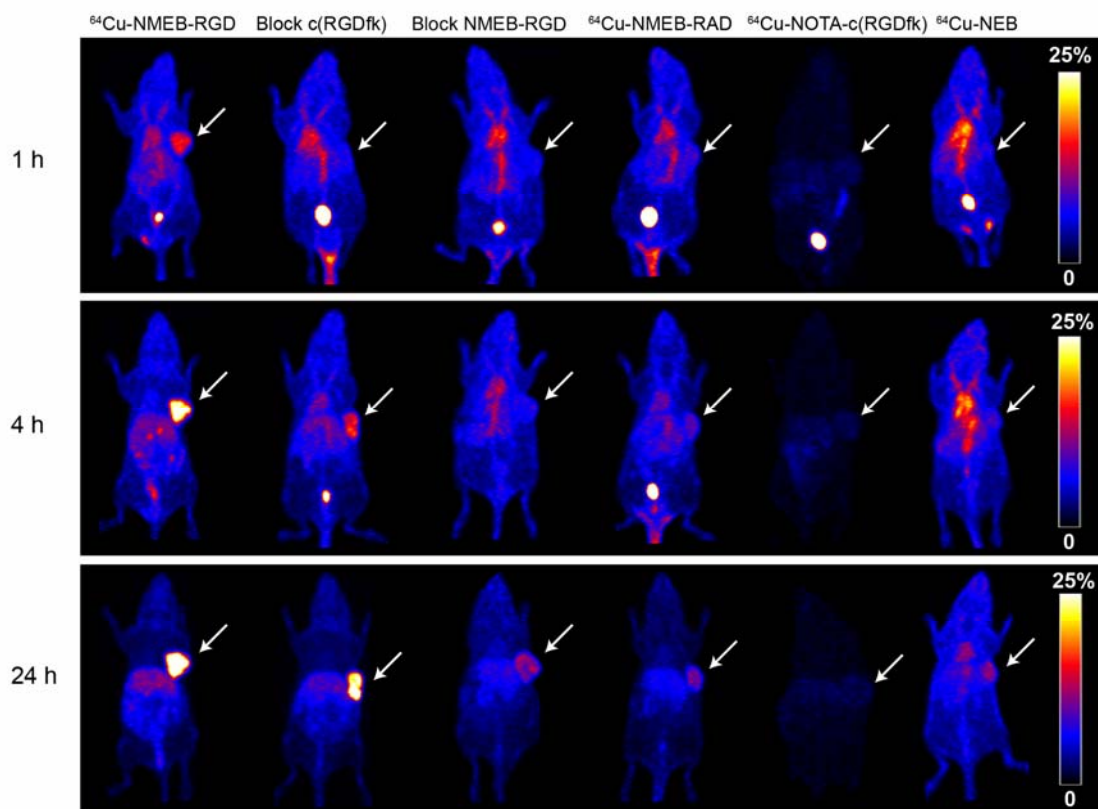


**Figure 3.** (A) Projection PET images of U87MG xenografts injected with 3.7 MBq of  $^{64}\text{Cu}$ -NMEB-RGD ( $n = 6$ ),  $^{64}\text{Cu}$ -NMEB-RGD co-injected with 400  $\mu\text{g}$  RGD ( $n = 4$ ),  $^{64}\text{Cu}$ -NMEB-RGD co-injected with 400  $\mu\text{g}$  unlabeled NMEB-RGD ( $n = 3$ ),  $^{64}\text{Cu}$ -NMEB-RAD ( $n = 4$ ),  $^{64}\text{Cu}$ -RGD ( $n = 4$ ) and  $^{64}\text{Cu}$ -NEB ( $n = 4$ ) at 1, 4 and 24 h p.i. White arrows indicate the tumor location.

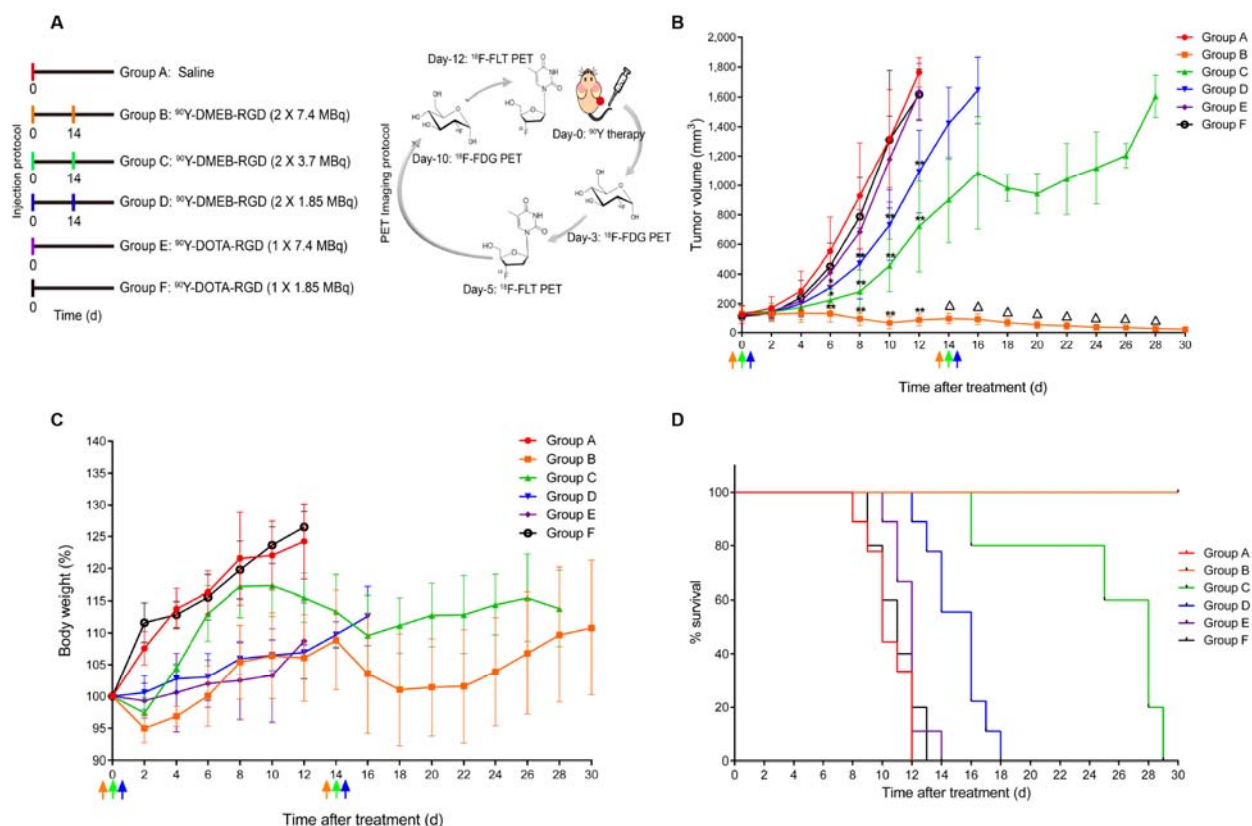


**Figure 4.** (A) Design of therapy protocol. (B) Tumor volume (C) body weight change and (D) survival analysis of mice (n = 5 - 8/group) injected with: saline (group A), 7.4 MBq of  $^{90}\text{Y}$ -DMEB-RGD (group B), 3.7 MBq of  $^{90}\text{Y}$ -DMEB-RGD (group C), 1.85 MBq of  $^{90}\text{Y}$ -DMEB-RGD (group D), 7.4 MBq of  $^{90}\text{Y}$ -DOTA-RGD (group E) and 1.85 MBq  $^{90}\text{Y}$ -DOTA-RGD (group F) at different days after treatment. Treatment initiated at day 0.  $**P < 0.01$  compared to groups A, E and F.

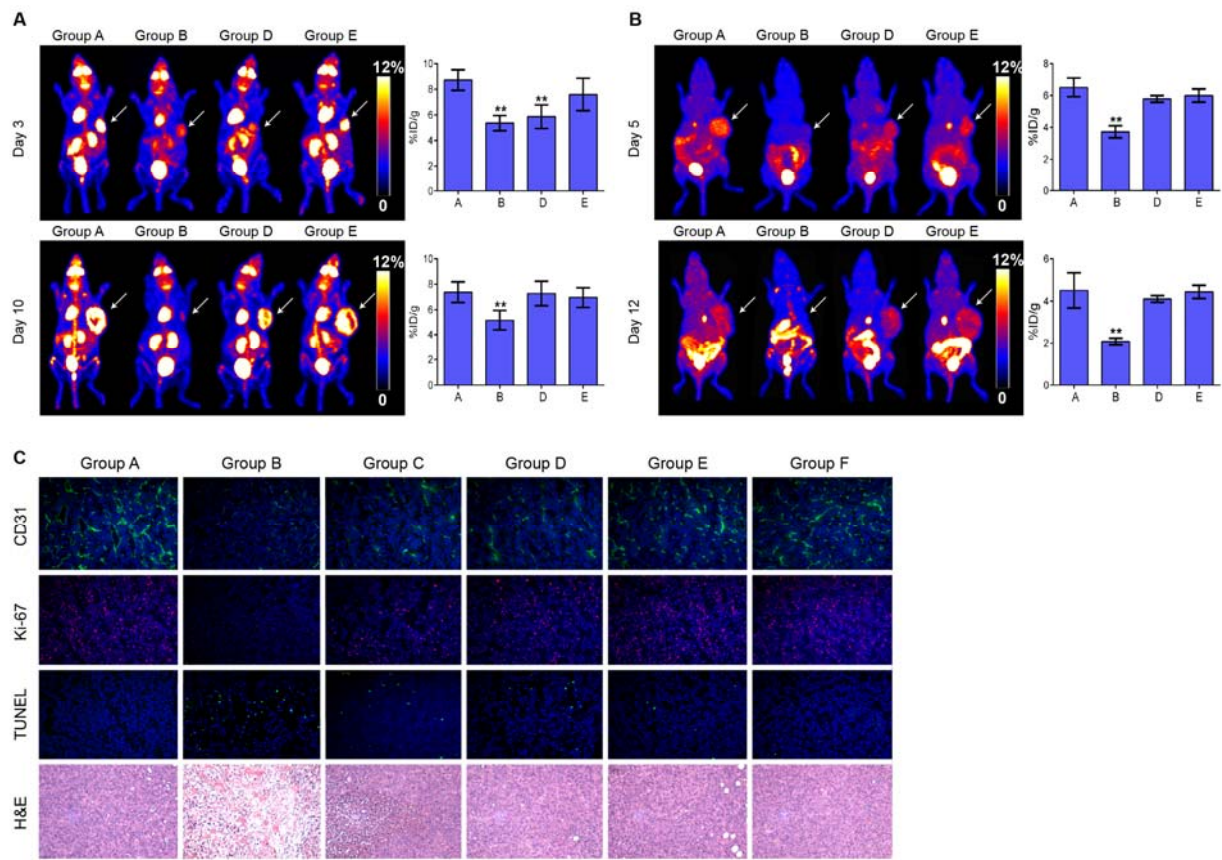


**Figure 5.** Projection PET images of mice injected with  $^{18}\text{F}$ -FDG (A top) 3 days and (A bottom) 10 days post-treatment and  $^{18}\text{F}$ -FLT (B top) 5 days and (B-bottom) 12 days post-treatment with: saline (group A), 7.4 MBq of  $^{90}\text{Y}$ -DMEB-RGD (group B), 1.85 MBq of  $^{90}\text{Y}$ -DMEB-RGD (group D) and 7.4 MBq of  $^{90}\text{Y}$ -DOTA-c(RGDfk) (group E). (C) Immunofluorescence staining of excised tumors for CD31 (vascularity), Ki-67 (proliferation) and TUNEL (apoptosis) and H&E after radiotherapy treatment was terminated.  $**P < 0.01$ .

## Supplemental Materials

### **Novel molecular “add-on” based on Evans Blue confers superior pharmacokinetics and transforms drugs to theranostic agents**

Haojun Chen<sup>1,2,\*</sup>, Orit Jacobson<sup>2,\*,§</sup>, Gang Niu<sup>2</sup>, Ido D. Weiss<sup>4</sup>, Dale O. Kiesewetter<sup>2</sup>, Yi Liu<sup>2</sup>, Ying Ma<sup>2</sup>, Hua Wu<sup>1,§</sup> and Xiaoyuan Chen<sup>2,§</sup>

1. Department of Nuclear Medicine, Xiamen Cancer Hospital of the First Affiliated Hospital of Xiamen University, Xiamen, China.
2. Laboratory of Molecular Imaging and Nanomedicine, National Institute of Biomedical Imaging and Bioengineering, National Institutes of Health, Bethesda, Maryland, USA.
3. Laboratory of Molecular Immunology, National Institute of Allergy and Infectious Diseases, National Institutes of Health, Bethesda, Maryland, USA.

§ Corresponding authors. Orit Jacobson (orit.jacobsonweiss@nih.gov); Hua Wu (wuhua1025@163.com); Xiaoyuan Chen (shawn.chen@nih.gov)

\* These authors contributed equally to this work.

## MATERIALS AND METHODS

### General

Boc-Lysine-Fmoc amino acid was purchased from Bachem. NOTA-bis(t-Bu ester) and DOTA-tris-(t-Bu ester) were purchased from Macrocyclics. N-succinimidyl S-acetylthioacetate (SATA) and PEG<sub>4</sub> biotinylation reagent were purchased from Thermo Fisher Scientific. Avidin-sepharose beads were acquired from GE Healthcare. Cyclic-(Arg-Gly-Asp-d-Phe-Lys) (RGD) peptide was purchased from C.S. Bio. All other solvents and chemicals were purchased from Sigma-Aldrich.

Analytical high performance liquid chromatography (HPLC) was done on Phenomenex Luna C8 column (5  $\mu$ m, 4.60 $\times$ 150 mm) with two gradient systems; *system 1* – gradient starting from 80% of solvent A (50mM NH<sub>4</sub>OAc) and 20% of solvent B (CH<sub>3</sub>CN) for 2 min and increasing to 90% of solvent B in 15 min at flow rate of 1 mL/min. *System 2* - gradient starting from 95% solvent A and 5% solvent B and changing to 65% solvent B at 35 min at flow rate of 1 mL/min. The ultraviolet (uv) absorbance was monitored at 254 and 600 nm. Compounds were purified on either Biotage purification system (C-18, 210  $\times$  25 mm) or Higgins column (C-18, 5 $\mu$ m, 250 $\times$ 20 mm) using gradient system 2 and flow rates of 25 or 12 mL/min respectively using a gradient similar to system 2 except change in the solvents [solvent A: 0.1% trifluoroacetic acid (TFA)/H<sub>2</sub>O, solvent B: 0.1% TFA/CH<sub>3</sub>CN]. LC-MS analysis was done similar to the reported procedure (1). <sup>64</sup>CuCl<sub>2</sub> was acquired from the NIH Cyclotron Facility. Radio-TLC was performed on an AR-2000 Bioscan scanner, using iTLC plates and 0.1M Citric acid pH 5 as a developing solvent. <sup>18</sup>F-FGD was purchased from Cardinal Health. <sup>18</sup>F-FLT was synthesized according to the known procedure (2).

Disclaimer: The NIH, its officers, and employees do not recommend or endorse any company, product, or service.

## Chemistry

Synthesis of EB-Lys-Boc. EB-NH<sub>2</sub> was synthesized according to the reported literature (1). To a solution of Boc-Lys-Fmoc (80-100 mM, 3.6 eq) in anhydrous N,N-dimethylformamide (DMF) were added (1-[bis(dimethylamino)methylene]-1H-1,2,3-triazolo[4,5-b]pyridinium 3-oxide hexafluorophosphate) (HATU, 4.2 eq) as a solid under argon. The solution was stirred for 10 min at room temperature (RT). Then 10 eq of diisopropylethylamine (DIPEA) were added followed by addition of EB-NH<sub>2</sub> (11-17 mM, 1eq) in DMF. Progress of the reaction was monitored by analytical HPLC using system 1. The reaction was stirred overnight at RT. Retention time of EB-NH<sub>2</sub> was 7.7 min and conjugated EB-protected Lys was 11 min. After the reaction stirred overnight, HPLC indicated complete conversion. Piperidine (20% v/v) was added and the reaction was stirred for an additional hour in order to cleave the Fmoc protecting group. DMF was removed under high vacuum and the residue was re-dissolved in methanol/H<sub>2</sub>O (2:1) and purified on Biotage system. The collected fractions were re-injected onto an analytical HPLC and those displaying a purity greater than 90% were combined and lyophilized to provide the product in an isolated yield of 40%. EB-Lys-Boc retention time (r.t.) was 8.3 min (system 1) or 23.2 min (system 2). LC-MS analysis confirmed mass of 769 [M-H]<sup>-</sup>.

Synthesis of NOTA-EB-Lys-Boc. Reaction between EB-Lys-Boc and NOTA-bis(t-Bu ester) was done similar to the conditions described above in the presence of 4.2 eq HATU and 10 eq of base. Analytical HPLC system 2 confirmed purity > 90% with a r.t. of 29.3 min and mass of 1167 [M-H]<sup>-</sup> and an isolated yield of 65%.

Synthesis of NOTA-EB-Lys. Deprotection was done at RT using thioanisole:1,2-ethanedithiol:anisole:TFA (5:3:2:90) in a total volume of 2 mL. Completion of deprotection was monitored by HPLC (r.t. of 17.1 min). TFA was removed by Argon flow before purification. NOTA-EB-Lys was purified on Biotage system. LC-MS analysis confirmed mass of 954[M-H]<sup>-</sup> with an isolated yield of 88%.

Synthesis of NOTA-Maleimide-EB (NMEB). NOTA-EB-Lys (10-14 mM) was dissolved in DMF. Then 1.26 eq of triethylamine were added, followed by 1.26 eq of 3-(maleimido)propionic acid N-hydroxysuccinimide ester. The reaction was stirred for 2 h at RT. Purification was done on Higgins column. Analytical HPLC injection (system 2) showed purity >90% with a r.t. of 17.4 min and mass of 1105 [M-H]<sup>-</sup> and an isolated yield of 60%.

Synthesis of RGD-SH. 20-30 mg of RGD was dissolved in 1.5 mL of (100 mM) Na<sub>2</sub>HPO<sub>4</sub> pH 7.5. 1.3 eq. of SATA were dissolved in dimethylsulfoxide and added to the peptide solution. The solution was stirred for 1-1.5 h until HPLC showed complete conversion to the conjugated peptide. The solvent was removed by lyophilization overnight. Deprotection of the acetyl group was done using 70 mg hydroxylamine and 20 mg ethylenediaminetetraacetic acid in 0.1M borate buffer pH 8.6 and H<sub>2</sub>O (1:1) (in a total volume of 3 mL) for 1h at RT. Purification of RGD-SH was done on Higgins column. Re-injection of the pure peptide onto analytical HPLC showed purity greater than 90% with a r.t. of 17.3 min. LC-MS analysis was confirmed mass of 676 [M-H]<sup>-</sup>.

Synthesis of NMEB-RGD. NMEB (15-20 mM) was dissolved in 0.3 mL of de-gassed 0.1% sodium ascorbate (w/v) in phosphate buffer-saline (PBS). RGD-SH (1.1 eq) was dissolved in 50 µL of DMF and added to the NMEB solution. The reaction was stirred at RT for 2h. Purification

was done on Higgins system. NMEB-RGD r.t. was 17.54 min, chemical purity >90% and mass of 1783 [M-H]<sup>-</sup>.

Synthesis of DMEB was conducted in the same manner but using DOTA-tris (t-Bu ester) as a chelator, with HPLC r.t. of 17.8 min and mass of 1883.9 [MH]<sup>-</sup>.

## **Radiochemistry**

Labeling of NMEB-RGD: 10 µL of <sup>64</sup>CuCl<sub>2</sub> (1.5-2.2 GBq, 42-60 mCi) were diluted with 0.5 mL 0.4 M ammonium acetate pH 5.6. Then 0.37-0.74 GBq (10-20 mCi) were transferred into a vial containing the peptide (100 µg). The reaction was mixed for 30 min at 37°C and then tested for purity by either analytical HPLC system 1 (r.t. 6.37) or radioTLC. R<sub>f</sub> of free <sup>64</sup>Cu ~ 0.9 and R<sub>f</sub> of <sup>64</sup>Cu-NMEB-RGD ~ 0.1. Labeling of <sup>64</sup>Cu-RGD and <sup>64</sup>Cu-NEB was done at the same manner. Y-90 (Perkin-Elmer) labeling was done similarly to the conditions described above for <sup>64</sup>Cu using 370-444 mBq (10-12 mCi).

## **Evaluation In Vitro**

Measurement of Binding Affinity using Cell Binding Assay: NMEB-RGD cell binding assays were performed with U87MG human glioma cells in a 96-well membrane plate. Incubation was conducted in 200 µL containing 10<sup>5</sup> suspended cells in serum free medium or 1% (w/v) HSA, 0.0185 MBq of <sup>64</sup>Cu-RGD and different concentrations of RGD or NMEB-RGD peptides ranging from 0 - 5000 nM. The incubation was conducted at room temperature (RT) for 4 h. After the incubation time, the plate was washed three times with PBS. The radioactivity in each well was measured using a gamma-counter. IC<sub>50</sub> values were calculated by fitting the data with nonlinear regression using GraphPad Prism. Experiments were performed in quadruplicate.

It is important to note that the binding assay was done under conditions that are suboptimal due to the fact that  $^{64}\text{Cu}$ -RGD does not have high specific activity (SA) and some of the receptors might have been blocked. However no other  $\alpha_v\beta_3$  radioligand is commercially available.

*In vitro* albumin binding affinity of the NMEB-RGD was assessed *via* competition with  $^{64}\text{Cu}$ -NMEB-RGD on avidin-sepharose beads using biotinylated albumin. Biotinylation of human albumin was done using EZ-link PEG<sub>4</sub> biotinylation reagent according to the manufacturer's instructions. Briefly, beads were incubated with biotin-albumin for 1h and then extensively washed. The beads were incubated with radiolabeled  $^{64}\text{Cu}$ -NMEB-RGD and increasing concentrations (0.1 nM-10  $\mu\text{M}$ ) of unlabeled NMEB-RGD for 1 h and then extensively washed with binding buffer. Thereafter, the radioactivity bound to the beads was measured using a gamma-counter.

Cell uptake and internalization: For cell uptake and internalization studies, U87MG, MDA-MB-435 and HT-29 cells were seeded in 24-well plates at a density of  $10^5$  cells/well 24 h before the assay. The medium was removed and the cells were rinsed twice with PBS. Then, 0.5  $\mu\text{Ci}$ /well of  $^{64}\text{Cu}$ -NMEB-RGD were added in 0.5 mL of serum free medium or medium containing 1% HSA. The cells were incubated at 37 °C for 5, 30, 60, and 240 min. At each indicated time point, the medium was removed and cells were rinsed twice with 1 mL PBS and lysed by addition of 0.2 mL 0.1M NaOH. For internalization studies, after the removal of the medium at the indicate time point, the cells were incubated for 1 min with 0.5 mL of acid buffer (50 mM Glycine, 100 mM NaCl, pH 2.8). Then the acid buffer was removed and the cells were washed twice with 1 mL PBS, followed by addition of 0.1 M NaOH. Cell lysate was collected and the radioactivity was measured by a  $\gamma$ -

counter. The cell uptake and internalization values were normalized to the amount of added radioactivity. Each experiment was repeated twice in triplicate.

Stability studies in mouse serum. 7.4-11.1 MBq (0.2-0.3 mCi) of  $^{64}\text{Cu}$ -NMEB-RGD were incubated with 0.5 mL of mouse serum for 1, 4, 8 and 24 h at 37°C. At each time point, an aliquot was analyzed by radioTLC to assess radiochemical stability.

Cell uptake of NMEB-RGD and FITC-Albumin.

$10^5$  cells were incubated (24 well plates) with a constant amount of FITC-albumin and increasing amounts of NMEB-RGD for 2 h. Thereafter, cells were washed with PBS and acquired using an LSR II flow cytometer. Cell fluorescence was expressed as mean fluorescent intensity (MFI). All cell uptake experiments were conducted in triplicate

Histopathologic Staining. For visualization of endothelial cells, integrin expression on both tumor vasculature and tumor cells, CD31, CD61 (murine integrin  $\beta_3$ ) or human integrin  $\alpha_v\beta_3$  immunofluorescence staining was chosen, respectively. The mouse anti-human integrin  $\alpha_v\beta_3$  antibody recognizes human integrin  $\alpha_v\beta_3$  and does not cross-react with murine integrin  $\alpha_v\beta_3$  of the tumor cells. Briefly, frozen tissue sections (5  $\mu\text{m}$ ) were fixed with cold acetone, rinsed with PBS and blocked with 1% bovine serum albumin solution for an hour at RT. The slides were incubated with 1:100 dilution of rat anti-mouse CD31, hamster anti-rat CD61 or mouse anti-human integrin  $\alpha_v\beta_3$  monoclonal antibody at room temperature overnight, and then incubated with 1:200 Alexa Fluor 488-labeled donkey anti-rat, Alexa Fluor 647-labeled anti-hamster, or Alexa Fluor 488-labeled anti-mouse secondary antibody, respectively. Samples were mounted with DAPI for

staining of cell nuclei. Fluorescence images were acquired with an epifluorescence microscope (200×; Olympus, X81). Images were acquired under the same conditions and displayed at the same scale.

#### *Histopathologic Staining after targeted radiotherapy*

U87MG tumor samples from Groups A-F were collected and sectioned. The CD31 staining procedure was the same as previously described. For Ki-67 staining, frozen tumor sections were fixed with cold acetone for 20 min and dried in the air for 30 min at room temperature. After blocking with 1% bovine serum albumin (BSA) for 30 min, slides were stained with Ki-67-specific monoclonal antibody (1:1000, Abcam) and then incubated with Cy-3-conjugated donkey anti-rabbit secondary antibody (1:200, Thermo Fisher Scientific). After being washed three times with PBS, samples were mounted with DAPI for staining of cell nuclei (Vector). Fluorescence images were acquired with an epifluorescence microscope (200X; Olympus, X81).

Immunofluorescent terminal deoxynucleotidyltransferase-mediated biotin-dUTP labeling (TUNEL) analysis was done by use of a commercial available kit (Roche Applied Science). According to the manufacturer's specifications, samples were fixed with 10% formalin and permeabilized by incubation with 0.1% Triton for 2 min on ice. After fixation and permeabilization, 50 µL of TUNEL reaction mixture were added on the samples. The slides were then incubated in a humidified atmosphere for 60 min at 37°C in the dark. After rinsing with PBS and mounting with DAPI (Vector), samples were observed under an epifluorescence microscope using GFP channel. Staining of human tissue was done by Histoserv, Inc. using sc-7312 antibody (Santa Cruz biotechnology, Inc.) H&E staining for mice tissues was also conducted by Histoserv, Inc.

## **Evaluation *In Vivo***

*Stability assays in FVB mice.* FVB mice were injected with 3.7 MBq (100  $\mu$ Ci) of  $^{64}\text{Cu}$ -NMEB-RGD. At 1 and 4 h, mice (n=2) were euthanized and blood was withdrawn from the heart. The red blood cells were separated from the plasma using centrifugation (3500 rpm for 5 min). Then after, 0.2 mL from the plasma were diluted with cold methanol (1:1), vortex for 30 second and centrifuged for 5 min at 10,600g. The extracted supernatant was taken, filtered through 0.45  $\mu\text{m}$  filter, and injected into analytical HPLC using system 1.

*Tumor Model.* Female athymic nude mice (Harlan Laboratories) were housed in an animal facility under pathogen-free conditions. Tumor model was developed in 5 to 6 weeks old female athymic nude mice by injection of  $5 \times 10^6$  cells into their right shoulders. The mice underwent small-animal PET studies when the tumor volume reached 300  $\text{mm}^3$  (14-20 days after inoculation), and received  $^{90}\text{Y}$  radionuclide therapy when the tumor volume reached 150  $\text{mm}^3$  (10-14 days after inoculation).

*Biodistribution.* U87MG tumor xenografts injected with  $^{64}\text{Cu}$ -NMEB-RGD were sacrificed after 24 h time-point PET imaging. Blood, muscle, bone, liver, kidneys, spleen, intestine, heart and tumor were collected and wet-weighed. For mice bearing MDA-MB-435 and HT-29 tumor xenografts, blood, tumor and heart were collected and radioactivity assayed using a  $\gamma$ -counter. The results were expressed %ID/g.

## **REFERENCES**

1. Niu G, Lang L, Kiesewetter DO, et al. In vivo labeling of serum albumin for PET. *J Nucl Med.* 2014;55:1150-1156.
2. Martin SJ, Eisenbarth JA, Wagner-Utermann U, et al. A new precursor for the radiosynthesis of [ $^{18}\text{F}$ ]FLT. *Nucl Med Biol.* 2002;29:263-273.

## Supplemental Figure Legends

**Supplemental Figure 1.** Chemical structure of  $^{64}\text{Cu}$ -NMEB-RGD (contains EB entity for albumin binding and RGD peptide as integrin  $\alpha_v\beta_3$  positive),  $^{64}\text{Cu}$ -NEB (contains only EB part with no specificity to integrin  $\alpha_v\beta_3$ ),  $^{64}\text{Cu}$ -RGD (integrin  $\alpha_v\beta_3$  positive but does not have albumin binding) and  $^{64}\text{Cu}$ -NMEB-RAD (contains albumin motif, EB, and integrin  $\alpha_v\beta_3$  negative).

**Supplemental Figure 2.** Cell binding assay in U87MG cells using  $^{64}\text{Cu}$ -RGD as a competitor and 4h incubation time of DMEB-RGD (A) and (B) NMEB-RAD with or without 1% HSA.

**Supplemental Figure 3.** (A) Cell uptake of  $^{64}\text{Cu}$ -NMEB-RGD in MDA-MB-435 and HT-29 cells without HSA and with 1% HSA. Blocking studies were evaluated at 4 h. (B) Cell internalization of  $^{64}\text{Cu}$ -NMEB-RGD in MDA-MB-435 cell line (C) and HT-29 cell line. Green bars represent the internalized radiotracer and the blue bars represent surface bound  $^{64}\text{Cu}$ -NMEB-RGD. Blocking studies were evaluated at 4h.  $**P < 0.01$ . (D) Lack of internalization of FITC-albumin in the presence of increasing concentrations of NMEB-RGD with (upper) and without (lower) acid wash.

**Supplemental Figure 4.** (A) Stability of  $^{64}\text{Cu}$ -NMEB-RGD in mouse serum over time using radioTLC and in vivo in mice blood (B) analyzed by radioHPLC.

**Supplemental Figure 5.** (A) Immunofluorescence staining of CD31, CD61 (murine integrin  $\beta_3$ ) and human integrin  $\alpha_v\beta_3$  in frozen section slides of U87MG, MDA-MB-435 and HT29 xenografts. Magnification 200x. (B) Quantified uptake of  $^{64}\text{Cu}$ -NMEB-RGD in U87MG tumors. PET quantification was done as both mean tumor uptake and max tumor uptake to compensate for necrotic areas that might affect the calculated mean.

(C) Quantified results for PET presented in Fig. 3 at different time points.  $*P < 0.05$ ,  $**P < 0.01$ .

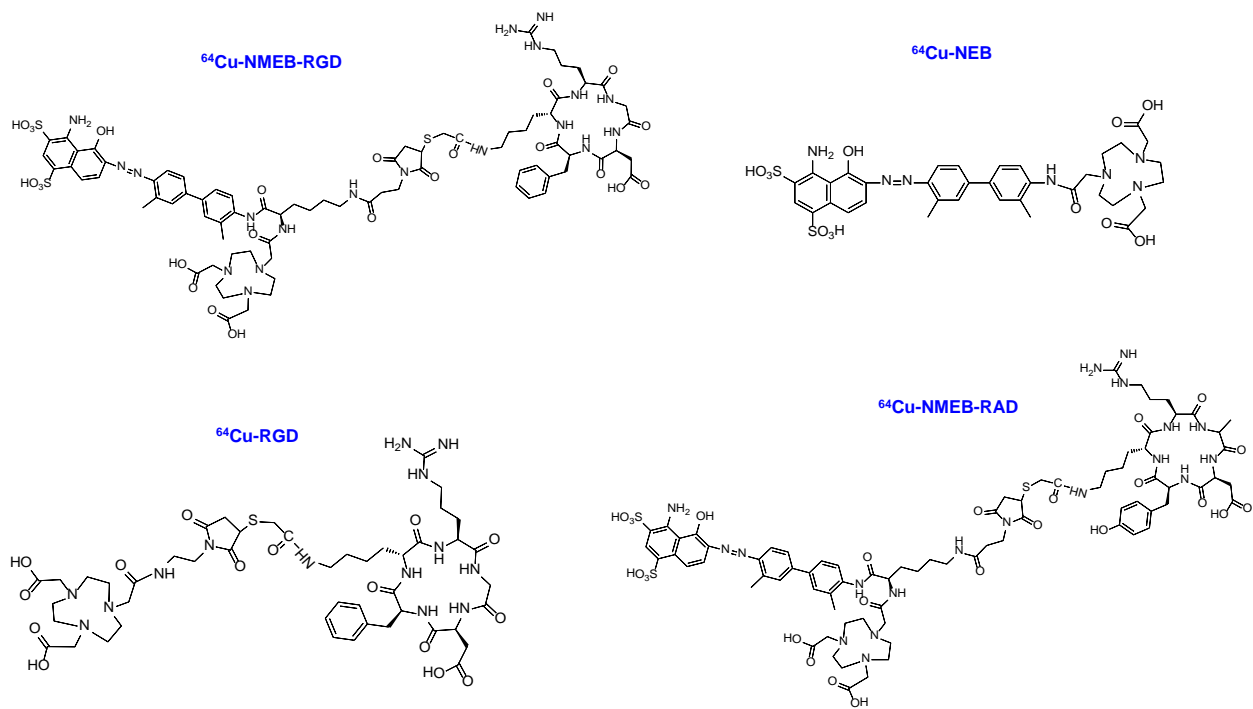
**Supplemental Figure 6.** Comparison of  $^{64}\text{Cu}$ -NMEB-RGD uptake in different tumors. (A) Projection PET images of mice bearing tumors with different integrin  $\alpha_v\beta_3$  levels injected with

3.7 MBq (100  $\mu$ Ci) of  $^{64}\text{Cu}$ -NMEB-RGD at 1, 4 and 24h p.i. White arrows indicate the tumor location. (B) PET quantification of the images in Fig. S11A.  $**P < 0.01$

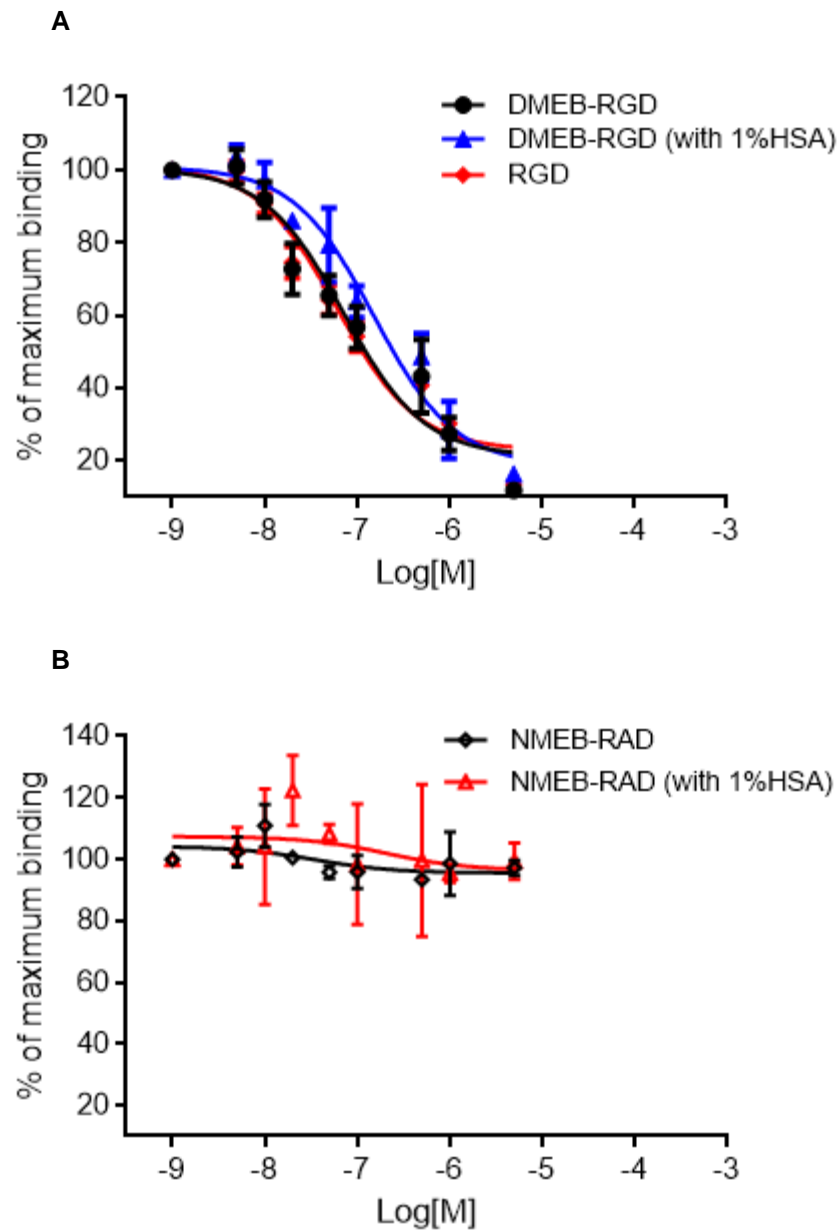
**Supplemental Figure 7.** (A) Biodistribution of  $^{64}\text{Cu}$ -NMEB-RGD in U87MG xenografts at 4 h post-injection. (B) Biodistribution comparison of blood, heart and tumor uptake of  $^{64}\text{Cu}$ -NMEB-RGD. (C)  $^{64}\text{Cu}$ -NEB in different integrin  $\alpha_v\beta_3$  expressing tumors.  $*P < 0.05$ ,  $**P < 0.01$ .

**Supplemental Figure 8. Cancer radiotherapy using  $^{90}\text{Y}$ -DMEB-RGD in HT-29 xenografts.**

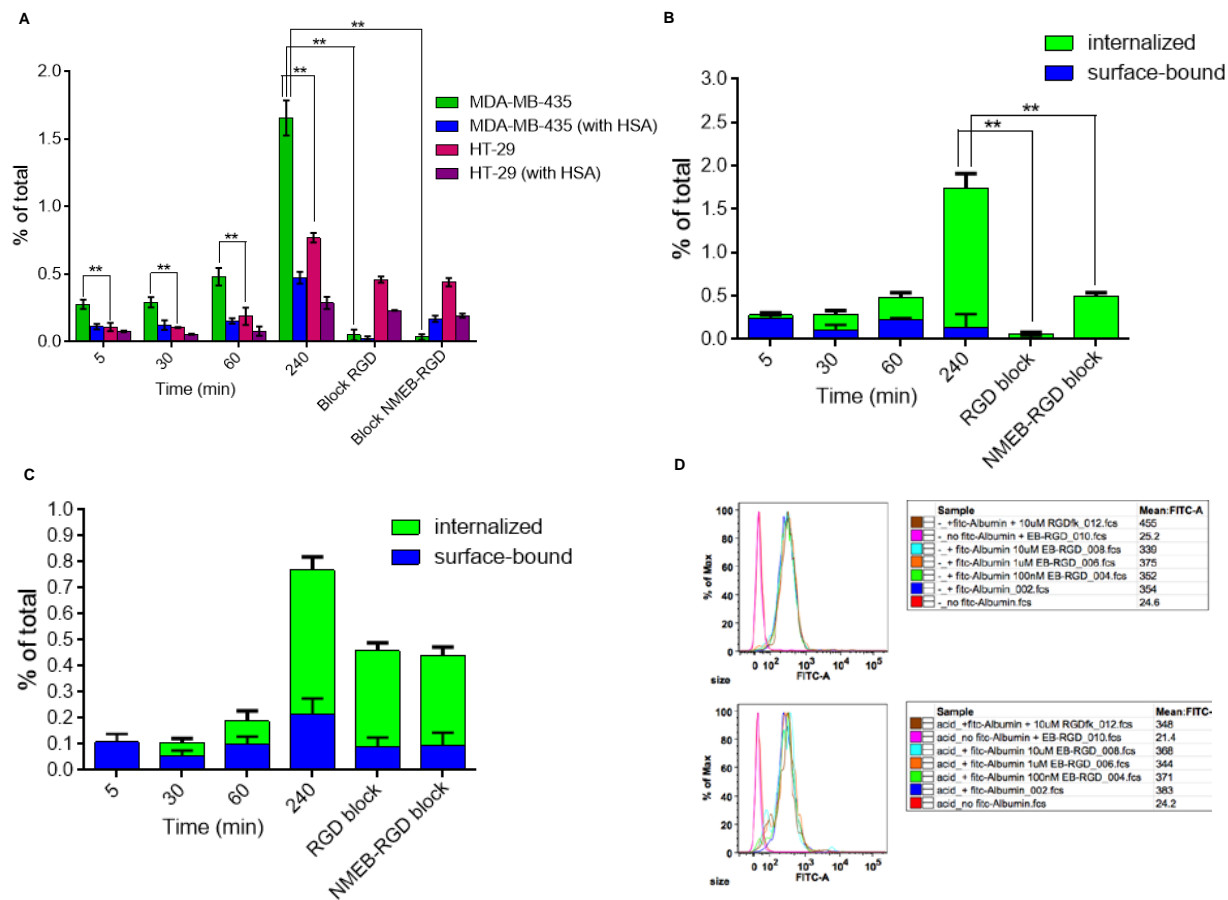
(A) Tumor volume growth and (B) body weight changes of mice injected with either; saline (control) and 200  $\mu$ Ci of  $^{90}\text{Y}$ -DMEB-RGD (treated). Treatment initiated at day 0.



**Supplemental Figure 1**

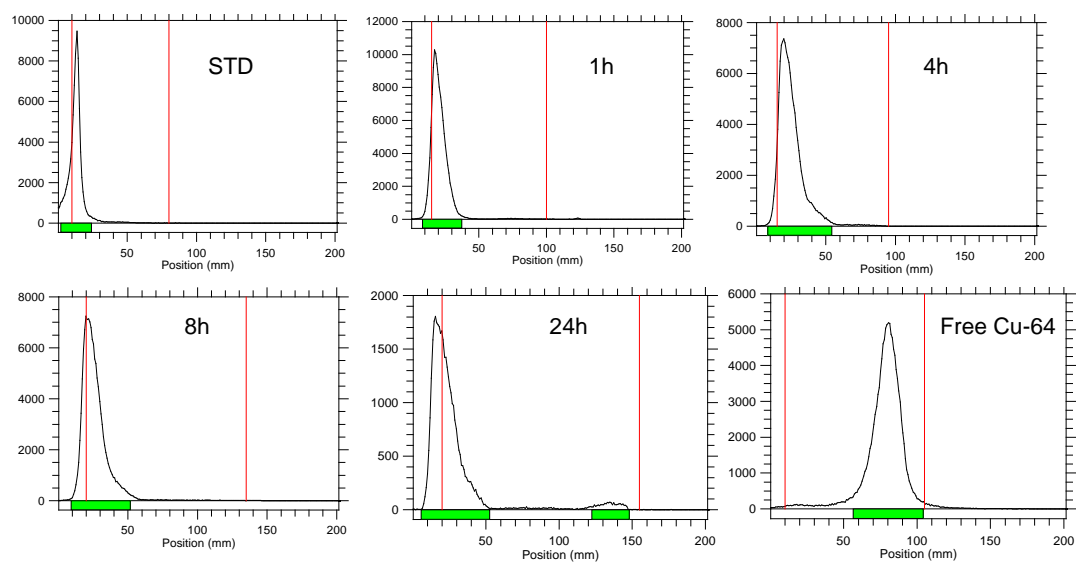


**Supplemental Figure 2**

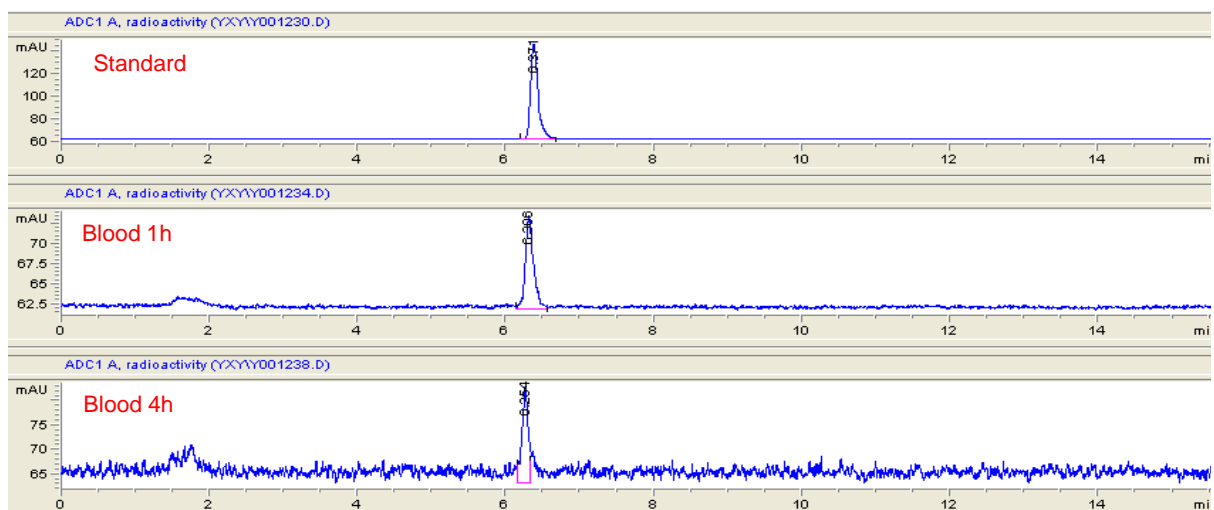


Supplemental Figure 3

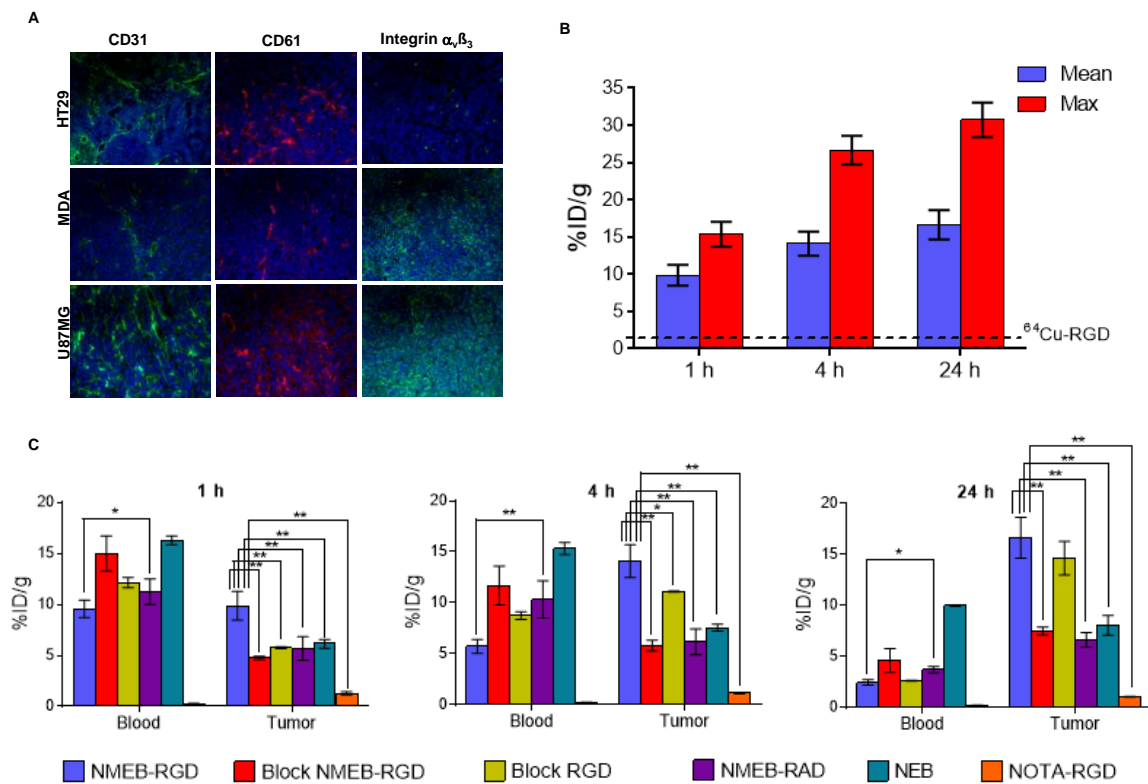
**A**



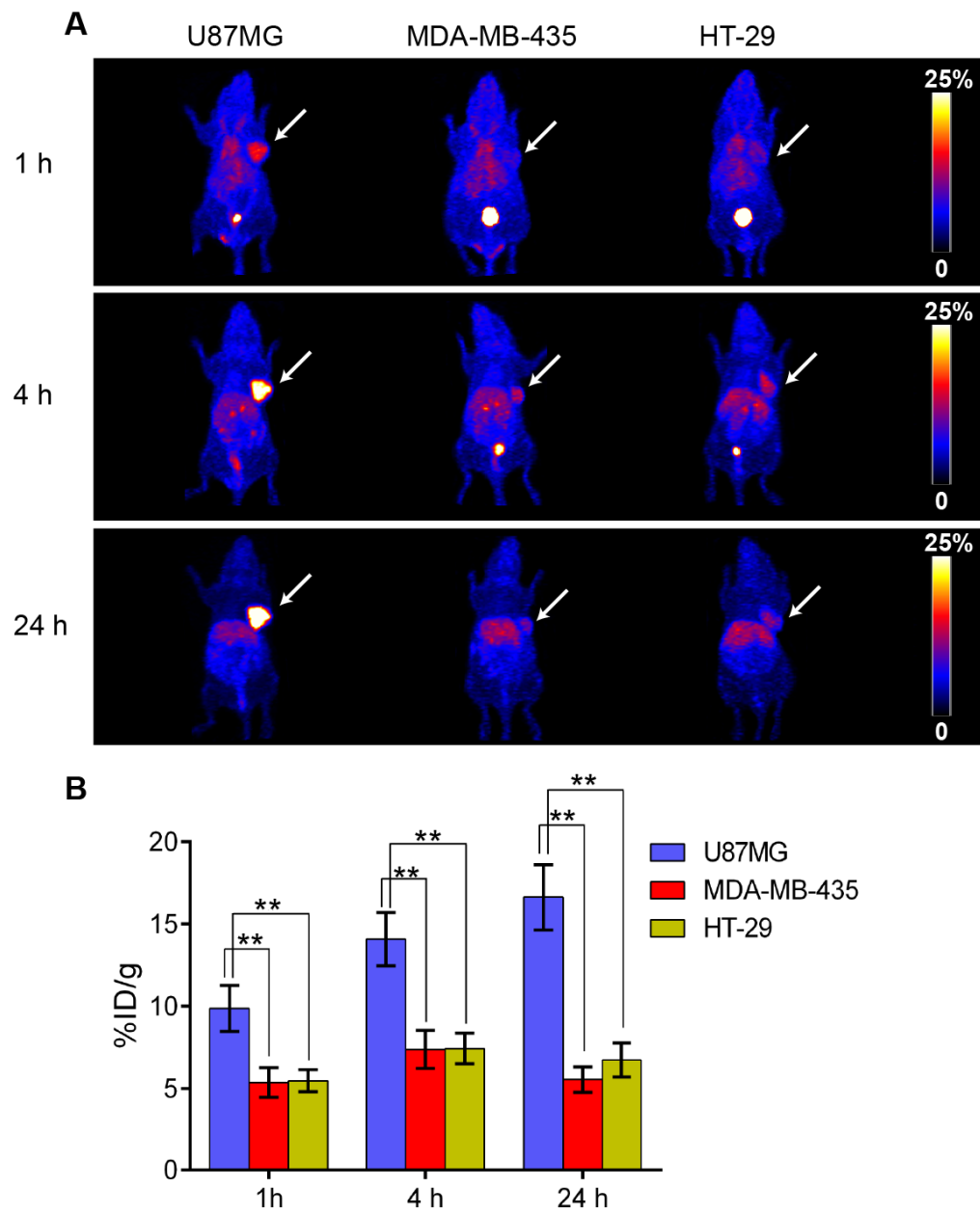
**B**



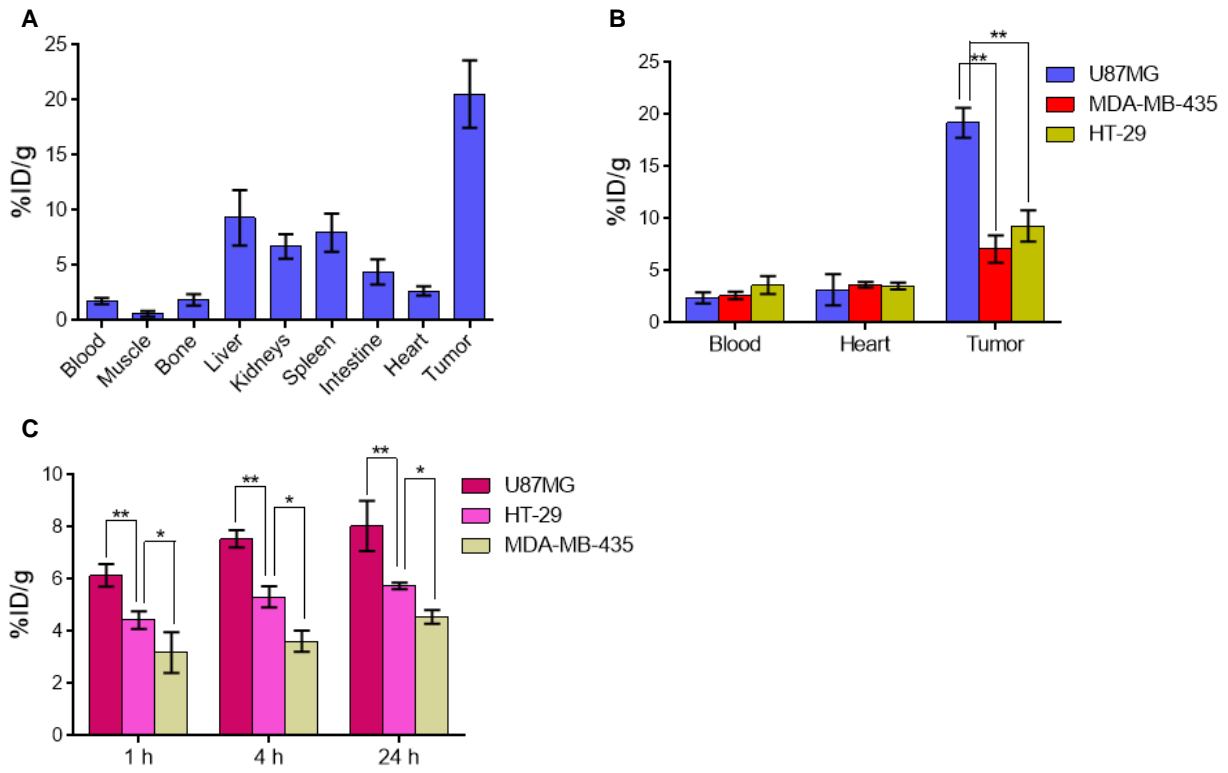
**Supplemental Figure 4**



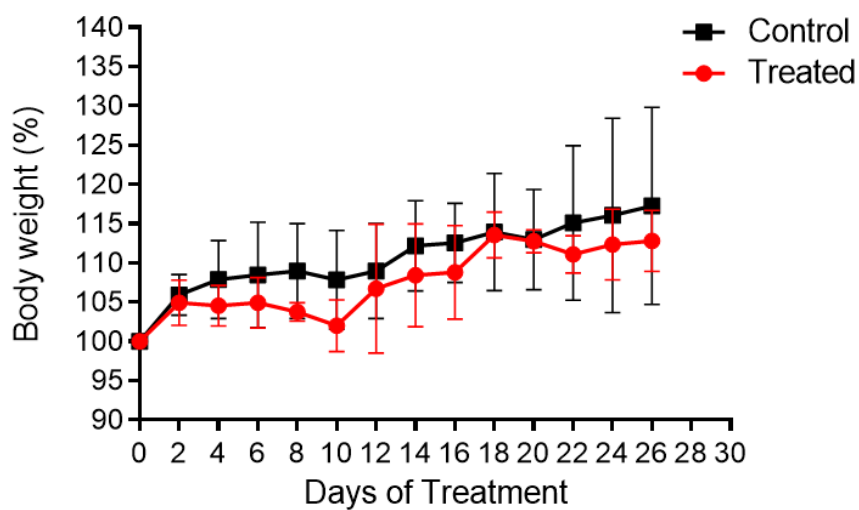
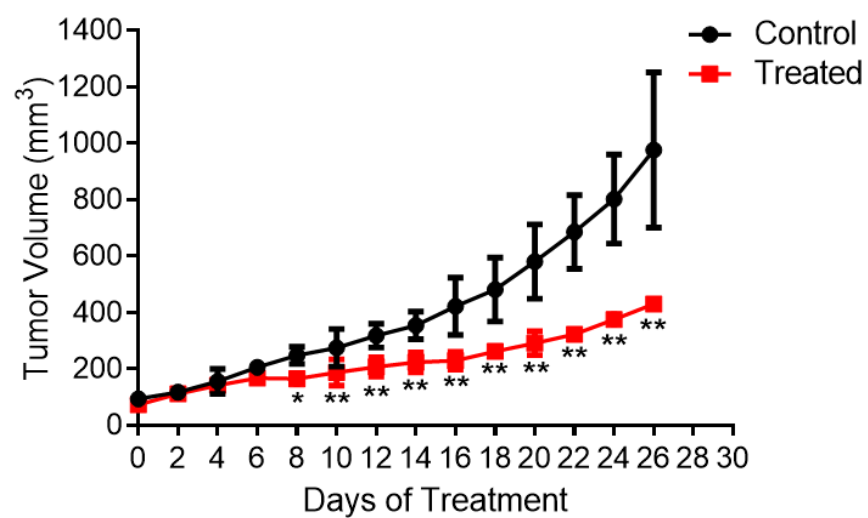
**Supplemental Figure 5**



Supplemental Figure 6



**Supplemental Figure 7**



Supplemental Figure 8